Journal of Magnetic Resonance **147,** 179–191 (2000)
doi:10.1006/jmre.2000.2177, available online at http://www.idealibrary.com on IDEAL®

# A Model for the Dynamics of Spins 3/2 in Biological Media: Signal Loss during Radiofrequency Excitation in Triple-Quantum-Filtered Sodium MRI[1]

Ileana Hancu,* Johan R. C. van der Maarel,† and Fernando E. Boada‡

*Department of Physics and ‡Department of Radiology, MR Research Center, University of Pittsburgh, Pittsburgh, Pennsylvania 15213; and †Leiden Institute of Chemistry, Gorlaeus Laboratories, Leiden University, Leiden, The Netherlands

Received March 10, 2000; revised July 13, 2000

**We have derived the differential equations that describe the dynamics of spin-3/2 nuclei in the presence of radiofrequency (RF) fields and both static and fluctuating quadrupolar interactions. The formalism presented was used to predict the sodium triple-quantum-filtered (TQ-filtered) signal loss in a whole-body scanner, where the widths of the hard 90° RF pulses are on the same order of magnitude as the transverse relaxation times. A small piece of bovine nasal cartilage, known for exhibiting residual quadrupolar splittings, was used to test the theory. The sample was modeled as consisting of small domains, each characterized by a static quadrupolar interaction constant, with an overall Gaussian distribution across the sample. An increase of about 15% in the TQ-filtered signal strength, as the 90° RF pulse width was decreased from 500 to 100 $\mu$s, was predicted and demonstrated experimentally for this particular sample.** 

*Key Words:* **relaxation; quadrupolar nuclei; cartilage; sodium; imaging.**

## INTRODUCTION

Sodium MRI has been proposed as a means to diagnose and monitor pathology in humans (*1, 2*). One of the main thrusts for the pursuit of sodium MRI lies in the large changes in sodium content that are associated with the development of pathology. In the brain, for example, there is a large concentration gradient across the cell membrane. This gradient results from the active maintenance of a relatively low intracellular sodium concentration (~10 mM in normal brain cells) against a very large extracellular sodium pool (with an average brain concentration of 140 mM). The large difference in sodium content between these two tissue compartments is of critical importance for the brain's function and, because of its large energetic cost, is highly sensitive to the changes in brain physiology that follow the onset of disease. Because the extracellular sodium content is in equilibrium with the plasma (which has a fixed sodium content of 140 mM), the intracellular compartment can exhibit very large (>100%), and distinctive, changes in sodium concentration during the course of disease. Therefore, a means for monitoring the intracellular sodium content *in vivo* using MRI could prove to be a very useful tool for the diagnosis and follow-up of disease in humans.

Different schemes have been proposed for separating the sodium NMR signal from the intra- and extracellular compartments (*3–8*). Among them, triple-quantum (TQ) filtered NMR techniques have received considerable attention because of their noninvasive nature and relatively simple implementation. Although the characteristics of the TQ-filtered sodium NMR signal have been well described in various organ systems using animal models (*9–11*), it is only recently that *in vivo* TQ-filtered sodium MRI in humans has been demonstrated (*12, 13*). This stems from the relatively weak nature of the TQ-filtered sodium NMR signal, which requires the use of efficient imaging schemes (*14*) in order to produce images of acceptable signal-to-noise ratio (>15:1) in reasonable imaging times (<20 min).

As previously demonstrated (*13*), the TQ-filtered sodium signal has a strong dependence on the spatial distribution of the radiofrequency (RF) field and, in particular, can be better observed in whole-body scanners if no refocusing pulses are used. This approach is a major departure from that used previously in small bore systems (*10, 15*), where the use of refocusing pulses was advocated as a means to reduce signal loss due to main magnetic field inhomogeneities. The use of this approach is justified by the fact that over a large (>15 cm) field of view (FOV), the signal loss due to inhomogeneous RF excitation typically exceeds that arising because of main magnetic field inhomogeneities (*13*). A further consequence of the use of TQ-filtered sodium MRI over large FOVs is that the RF pulses required to produce a 90° nutation are much larger than those employed in small bore systems (i.e., 500 $\mu$s vs 40 $\mu$s). Such long RF pulses could give rise to unwanted signal loss during RF excitation, which is difficult to minimize due to the hardware limitations of whole-body scanners and/or patient safety concerns.

[1] This work was supported, in part, by the Whitaker Foundation and by the PHS Grant R01 HL64205-1.



1090-7807/00 $35.00

The dynamics of a spin-3/2 system cannot be described by the classical Bloch equations, and there exists no previously published theoretical model to estimate the signal loss in such conditions. As the signal-to-noise (SNR) of the TQ-filtered sodium images is low, and the signal loss during RF excitation is difficult to minimize due to hardware constraints, a theoretical model for its calculation could be an invaluable tool for the optimization of TQ-filtered sodium MRI applications.

We present a theoretical model for the calculation of TQ-filtered sodium MRI signal loss during RF excitation in biological media. As part of the model, we derive the differential equations that describe the evolution of a pool of spin-3/2 nuclei (simulating the biological tissue) in the presence of a RF field and static and fluctuating quadrupolar interactions. Only the limiting case for which the correlation time of the fluctuations is smaller than the inverse of the quadrupole splitting is considered. The pool of spins is modeled as composed of a multitude of domains, each characterized by a static quadrupolar interaction parameter, with an overall Gaussian distribution (average $\bar{\omega}_Q$ and standard deviation $\sigma$) across the sample. The fluctuating interactions induce relaxation. Through the use of irreducible tensor operators and following the formalism developed for spin-1 nuclei (*16*), it is shown that the equation of evolution can be decomposed into two sets of differential equations, which evolve independently and are coupled at a change of RF phase. These equations are solved for static quadrupolar interaction constants in the range $[\bar{\omega}_Q - 3\sigma, \bar{\omega}_Q + 3\sigma]$, and the results are added together using the underlying Gaussian distribution, so that the macroscopic behavior of the spin system can be predicted.

Using this model, the TQ-filtered sodium MRI signal loss during RF excitation was predicted for a sample of bovine nasal cartilage. The experimental data, collected using a NMR spectrometer due to the capability of achieving a large range of pulse widths (12 $\mu$s to 1 ms), was found to agree very well with the theoretical predictions. The results from these investigations suggest that the signal loss during RF excitation in TQ-filtered sodium MRI using whole-body scanners is not likely to exceed 15%.

## THEORY

### 1. Differential Equations

The dynamics of the system of spins is described by the evolution of the density operator. All calculations reported here are done in the Larmor frequency rotating frame, indicated by an asterisk. The time evolution of the density matrix under a static Hamiltonian $H_S^*$ (time-independent) and a fluctuating part $H_{QF}^*(t)$ is given by the master equation (*17*)

$$\frac{d\sigma^*}{dt} = -i[H_S^*, \sigma^*] + f(\sigma^*). \quad [1]$$

The relaxation term $f(\sigma^*)$ is expressed as

$$f(\sigma^*) = -\int_0^\infty \langle [H_{QF}^*(t), [e^{-iH_S^*\tau} H_{QF}^*(t-\tau) e^{iH_S^*\tau}, \sigma^*(t)]] \rangle d\tau. \quad [2]$$

Throughout this work, the density operator and the Hamiltonians are represented in terms of irreducible tensor operators (*18*). Symmetric and antisymmetric combinations are defined as

$$T_{lm}(s) = (1/\sqrt{2})(T_{l-m} + T_{lm})$$
$$T_{lm}(a) = (1/\sqrt{2})(T_{l-m} - T_{lm}). \quad [3]$$

Orthonormal tensor operators $\hat{T}_{lm}$ are also introduced, being more convenient to use. They are related to their $T_{lm}$ counterparts (*18*) ($\hat{T}_{lm} = a_l T_{lm}$) and fulfill the orthogonality relationship $\mathrm{Tr}\{\hat{T}_{lm}\hat{T}^+_{l'm'}\} = \delta_{ll'}\delta_{mm'}$, with $\hat{T}^+_{lm} = (-1)^m \hat{T}_{l-m}$. For spin-3/2, the coefficients $a_l$ have the values 1/2 ($l = 0$), $1/\sqrt{5}$ ($l = 1$), $(1/2)\sqrt{2/3}$ ($l = 2$), and $(1/3)\sqrt{2}$ ($l = 3$). Symmetric and antisymmetric combinations of unit tensor operators are defined analogously to Eq. [3]. For spins-3/2, 16 basis operators are needed to describe the spin dynamics: $\hat{T}_{00}$ (the identity), $\hat{T}_{10}$ (longitudinal magnetization), $\hat{T}_{11}(a)$ and $\hat{T}_{11}(s)$ (proportional to the *x*- and *y*-magnetization, respectively), $\hat{T}_{20}$ (quadrupolar spin polarization), $\hat{T}_{21}(s)$ and $\hat{T}_{21}(a)$ (second-order single-quantum coherences), $\hat{T}_{22}(s)$ and $\hat{T}_{22}(a)$ (second-order double-quantum coherences), $\hat{T}_{30}$ (octopolar spin polarization), $\hat{T}_{31}(s)$ and $\hat{T}_{31}(a)$ (third-order single-quantum coherences), $\hat{T}_{32}(s)$ and $\hat{T}_{32}(a)$ (third-order double-quantum coherences), and $\hat{T}_{33}(s)$ and $\hat{T}_{33}(a)$ (third-order triple-quantum coherences).

With respect to the Larmor frequency rotating frame, the Zeeman Hamiltonian ($H_z = \omega_0 I_z = \omega_0 T_{10}$) vanishes. The static Hamiltonian in the master equation is then given by the sum of the static quadrupolar and RF contributions:

$$H_S^* = H_{QS}^* + H_1^*. \quad [4]$$

Denoting $\omega_Q$ as the residual static quadrupolar interaction parameter, the static quadrupolar Hamiltonian is expressed as

$$H_{QS}^* = \frac{1}{6}\omega_Q[3I_z^2 - I(I+1)] = \omega_Q\sqrt{\frac{1}{6}}T_{20} = \omega_Q\hat{T}_{20}. \quad [5]$$

The RF field is applied exactly on resonance along the *x*-axis and has the form

$$H_1^* = \omega_1 I_x = \omega_1 T_{11}(a) = \sqrt{5}\,\omega_1 \hat{T}_{11}(a). \quad [6]$$

If a phase is associated with the hard pulse, this will be reflected

in a change of base, not in the form of the RF Hamiltonian. Assuming that a hard pulse of phase $\Phi_1$ is followed by a hard pulse of phase $\Phi_2$, the change in base can be expressed as

$$T_{lm}^{(a)}(a) = T_{lm}^{(b)}(a)\cos[m(\Phi_2 - \Phi_1)] + iT_{lm}^{(b)}(s)\sin[m(\Phi_2 - \Phi_1)], \quad [7a]$$

$$T_{lm}^{(a)}(s) = T_{lm}^{(b)}(s)\cos[m(\Phi_2 - \Phi_1)] + iT_{lm}^{(b)}(a)\sin[m(\Phi_2 - \Phi_1)]. \quad [7b]$$

The superscripts (b) and (a) stand for "before" and "after" the change of phase.

The zero-average fluctuating quadrupolar interaction can be expressed as

$$H_{QF}^{*}(t) = C_Q \sum_{m=-2}^{2} (-1)^m T_{2m} e^{im\omega_0 t}[F_{2-m}(t) - \langle F_{2-m}\rangle]. \quad [8]$$

Here, $C_Q = \sqrt{6}/eQ/(2I(2I-1)\hbar) = eQ/(\hbar\sqrt{6})$ ($Q$ is the quadrupolar moment of the nucleus and the other symbols have their usual meaning), the electric field gradient tensor components, $F_{2m}$, are defined elsewhere (*16*), and $\langle F_{2m}\rangle$ represents their average value.

*(a) Evolution Neglecting of Relaxation*

Using Eqs. [5] and [6] to express the static Hamiltonian and neglecting the relaxation contribution, the master equation becomes

$$\frac{d\sigma^*}{dt} = -i[\omega_Q \hat{T}_{20} + \sqrt{5}\,\omega_1 \hat{T}_{11}(a),\ \sigma^*]. \quad [9]$$

With the commutation relations (*18*), Eq. [9] reduces to two sets of coupled differential equations. The first one is

$$\frac{d}{dt}\begin{pmatrix} \hat{T}_{11}(a) \\ \hat{T}_{20} \\ \hat{T}_{21}(s) \\ \hat{T}_{22}(s) \\ \hat{T}_{31}(a) \\ \hat{T}_{32}(a) \\ \hat{T}_{33}(a) \end{pmatrix} = \begin{pmatrix} 0 & 0 & i\sqrt{3/5}\,\omega_Q & 0 & 0 & 0 & 0 \\ 0 & 0 & -i\sqrt{3}\,\omega_1 & 0 & 0 & 0 & 0 \\ i\sqrt{3/5}\,\omega_Q & -i\sqrt{3}\,\omega_1 & 0 & -i\omega_1 & i\sqrt{2/5}\,\omega_Q & 0 & 0 \\ 0 & 0 & -i\omega_1 & 0 & 0 & i\omega_Q & 0 \\ 0 & 0 & i\sqrt{2/5}\,\omega_Q & 0 & 0 & -i\sqrt{5/2}\,\omega_1 & 0 \\ 0 & 0 & 0 & i\omega_Q & -i\sqrt{5/2}\,\omega_1 & 0 & -i\sqrt{3/2}\,\omega_1 \\ 0 & 0 & 0 & 0 & 0 & -i\sqrt{3/2}\omega_1 & 0 \end{pmatrix} \begin{pmatrix} \hat{T}_{11}(a) \\ \hat{T}_{20} \\ \hat{T}_{21}(s) \\ \hat{T}_{22}(s) \\ \hat{T}_{31}(a) \\ \hat{T}_{32}(a) \\ \hat{T}_{33}(a) \end{pmatrix}, \quad [10a]$$

with the second one being

$$\frac{d}{dt}\begin{pmatrix} \hat{T}_{10} \\ \hat{T}_{11}(s) \\ \hat{T}_{21}(a) \\ \hat{T}_{22}(a) \\ \hat{T}_{30} \\ \hat{T}_{31}(s) \\ \hat{T}_{32}(s) \\ \hat{T}_{33}(s) \end{pmatrix} = \begin{pmatrix} 0 & -i\omega_1 & 0 & 0 & 0 & 0 & 0 & 0 \\ -i\omega_1 & 0 & i\sqrt{3/5}\,\omega_Q & 0 & 0 & 0 & 0 & 0 \\ 0 & i\sqrt{3/5}\,\omega_Q & 0 & -i\omega_1 & 0 & i\sqrt{2/5}\,\omega_Q & 0 & 0 \\ 0 & 0 & -i\omega_1 & 0 & 0 & 0 & i\omega_Q & 0 \\ 0 & 0 & 0 & 0 & 0 & -i\sqrt{6}\,\omega_1 & 0 & 0 \\ 0 & 0 & i\sqrt{2/5}\,\omega_Q & 0 & -i\sqrt{6}\,\omega_1 & 0 & -i\sqrt{5/2}\,\omega_1 & 0 \\ 0 & 0 & 0 & i\omega_Q & 0 & -i\sqrt{5/2}\,\omega_1 & 0 & -i\sqrt{3/2}\,\omega_1 \\ 0 & 0 & 0 & 0 & 0 & 0 & -i\sqrt{3/2}\,\omega_1 & 0 \end{pmatrix} \begin{pmatrix} \hat{T}_{10} \\ \hat{T}_{11}(s) \\ \hat{T}_{21}(a) \\ \hat{T}_{22}(a) \\ \hat{T}_{30} \\ \hat{T}_{31}(s) \\ \hat{T}_{32}(s) \\ \hat{T}_{33}(s) \end{pmatrix}. \quad [10b]$$

*(b) Relaxation Effects*

Using the present formalism, relaxation effects can be easily incorporated into the differential equations (through the addition of the relaxation contribution to the master equation). By neglecting the terms oscillating with multiples of Larmor frequency and using Eq. [8], Eq. [2] transforms to

$$f(\sigma^*) = -C_Q^2 \sum_{m=-2}^{2} \int_0^{\infty} [T_{2m}, [e^{-iH_S^*\tau} T_{2m}^{+} e^{iH_S^*\tau}, \sigma^*(t)]] \times \langle [F_{2m}^*(t) - \langle F_{2m}^*\rangle] \times [F_{2m}(t-\tau) - \langle F_{2m}\rangle]\rangle e^{im\omega_0\tau} d\tau. \quad [11]$$

The relaxation term reduces to a combination of spectral density

functions at a number of frequencies. The imaginary part of the spectral density functions results in very small, second-order, frequency shifts and in a weak coupling of the two sets of differential equations. We will ignore these dynamic frequency shifts, but they can easily be derived with the results collected in Tables 1–3. The real part of the spectral density function is defined as

$$J_m(\omega) = (6C_Q^2/2)\int_{-\infty}^{\infty} \langle [F^*_{2m}(t) - \langle F^*_{2m}\rangle] \times [F_{2m}(t-\tau) - \langle F_{2m}\rangle]\rangle e^{i\omega\tau} d\tau. \quad [12a]$$

If the correlation function is taken to be single-exponential with a correlation time $\tau_c$, the spectral density function takes the Lorentzian form

$$J_m(\omega) = (eQ/\hbar)^2/20\langle (V_{zz} - \langle V_{zz}\rangle)^2\rangle \tau_c/(1 + \omega^2\tau_c^2). \quad [12b]$$

causing the loss of correlation. For systems of aquo cations in tissue, there is evidence (*19–21*) that there are at least two correlation times. The one (very short) correlation time for the aquo cation itself will persist and, in addition, there will be a longer correlation time associated with fluctuations in the macromolecular environment. Accordingly, we have considered the spectral density functions to be expressed as a sum of at least two Lorentzians, each characterized by a correlation time and a mean-square quadrupole coupling constant.

The function $f(\sigma^*)$ includes terms proportional to $J_m(m\omega_0 \pm k_i)$, where the shift $\pm k_i$ is due the presence of $H^*_S$ ($k_i$ are the 15 eigenvalues of the matrices in Eqs. [10a] and [10b]). Since the Larmor frequency, $\omega_0$, is generally much larger than any of the frequencies $k_i$, for $m \neq 0$, $J_m(m\omega_0 \pm k_i) \approx J_m(m\omega_0)$, and $H^*_S$ can be neglected in Eq. [11]. The term with $m = 0$ will be treated separately.

*(i) $m \neq 0$ terms.* The time evolution of the density matrix under relaxation, considering only the effect of the $m = \pm 2$ and $m = \pm 1$ terms, is described by the following set of differential equations:
Here, $J_1 = J_1(\omega_0)$ and $J_2 = J_2(2\omega_0)$.

$$\frac{d}{dt}\begin{pmatrix} \hat{T}_{11}(a) \\ \hat{T}_{20} \\ \hat{T}_{21}(s) \\ \hat{T}_{22}(s) \\ \hat{T}_{31}(a) \\ \hat{T}_{32}(a) \\ \hat{T}_{33}(a) \end{pmatrix} = -\begin{pmatrix} J_1 + 2/5J_2 & 0 & 0 & 0 & -\sqrt{6}/5J_2 & 0 & 0 \\ 0 & 2J_1 + 2J_2 & 0 & 0 & 0 & 0 & 0 \\ 0 & 0 & J_1 + 2J_2 & 0 & 0 & 0 & 0 \\ 0 & 0 & 0 & 2J_1 + J_2 & 0 & 0 & 0 \\ -\sqrt{6}/5J_2 & 0 & 0 & 0 & J_1 + 3/5J_2 & 0 & 0 \\ 0 & 0 & 0 & 0 & 0 & J_2 & 0 \\ 0 & 0 & 0 & 0 & 0 & 0 & J_1 + J_2 \end{pmatrix} \begin{pmatrix} \hat{T}_{11}(a) \\ \hat{T}_{20} \\ \hat{T}_{21}(s) \\ \hat{T}_{22}(s) \\ \hat{T}_{31}(a) \\ \hat{T}_{32}(a) \\ \hat{T}_{33}(a) \end{pmatrix} \quad [13a]$$

and

$$\frac{d}{dt}\begin{pmatrix} \hat{T}_{10} \\ \hat{T}_{11}(s) \\ \hat{T}_{21}(a) \\ \hat{T}_{22}(a) \\ \hat{T}_{30} \\ \hat{T}_{31}(s) \\ \hat{T}_{32}(s) \\ \hat{T}_{33}(s) \end{pmatrix} = -\begin{pmatrix} 2/5J_1 + 8/5J_2 & 0 & 0 & 0 & 4/5J_1 - 4/5J_2 & 0 & 0 & 0 \\ 0 & J_1 + 2/5J_2 & 0 & 0 & 0 & -\sqrt{6}/5J_2 & 0 & 0 \\ 0 & 0 & J_1 + 2J_2 & 0 & 0 & 0 & 0 & 0 \\ 0 & 0 & 0 & 2J_1 + J_2 & 0 & 0 & 0 & 0 \\ 4/5J_1 - 4/5J_2 & 0 & 0 & 0 & 8/5J_1 + 2/5J_2 & 0 & 0 & 0 \\ 0 & -\sqrt{6}/5J_2 & 0 & 0 & 0 & J_1 + 3/5J_2 & 0 & 0 \\ 0 & 0 & 0 & 0 & 0 & 0 & J_2 & 0 \\ 0 & 0 & 0 & 0 & 0 & 0 & 0 & J_1 + J_2 \end{pmatrix} \begin{pmatrix} \hat{T}_{10} \\ \hat{T}_{11}(s) \\ \hat{T}_{21}(a) \\ \hat{T}_{22}(a) \\ \hat{T}_{30} \\ \hat{T}_{31}(s) \\ \hat{T}_{32}(s) \\ \hat{T}_{33}(s) \end{pmatrix}. \quad [13b]$$

Here, the *zz*-component of the electric field gradient (EFG) is denoted by $V_{zz}$ and $\langle V_{zz}\rangle$ represents its residual average over all the sites that the counterion accesses in times less than the inverse of the quadrupolar splittings and/or linewidths over these sites. There are often several independent processes at different time scales

*(ii) $m = 0$ terms.* For $m = 0$, the function $f(\sigma^*)$ has to be fully evaluated. The appendix presents the necessary intermediate steps leading to the differential equations describing the effect of the slowly fluctuating electric field gradients. Apart from the high-frequency contributions $J_1(\omega_0)$ and $J_2(2\omega_0)$, the

relaxation rates are sensitive to the spectral densities at frequencies 0, $\lambda_1$, and $\lambda_2$. The (low) frequencies $\lambda_1$ and $\lambda_2$ are related to both the residual quadrupolar coupling and the RF field strength according to expression [A2] in the Appendix. However, since throughout this work we neglect any low-frequency dispersion of the order of $\lambda_{1,2}$, we assume that $J_0(0) \approx J_0(\lambda_1) \approx J_0(\lambda_2) = J_0$, and Eqs. [A5a] and [A5b] in the Appendix reduce to the much simpler form

$$\frac{d}{dt}\begin{pmatrix} \hat{T}_{11}(a) \\ \hat{T}_{20} \\ \hat{T}_{21}(s) \\ \hat{T}_{22}(s) \\ \hat{T}_{31}(a) \\ \hat{T}_{32}(a) \\ \hat{T}_{33}(a) \end{pmatrix} = -\begin{pmatrix} 3/5J_0 & 0 & 0 & 0 & \sqrt{6}/5J_0 & 0 & 0 \\ 0 & 0 & 0 & 0 & 0 & 0 & 0 \\ 0 & 0 & J_0 & 0 & 0 & 0 & 0 \\ 0 & 0 & 0 & J_0 & 0 & 0 & 0 \\ \sqrt{6}/5J_0 & 0 & 0 & 0 & 2/5J_0 & 0 & 0 \\ 0 & 0 & 0 & 0 & 0 & J_0 & 0 \\ 0 & 0 & 0 & 0 & 0 & 0 & 0 \end{pmatrix} \times \begin{pmatrix} \hat{T}_{11}(a) \\ \hat{T}_{20} \\ \hat{T}_{21}(s) \\ \hat{T}_{22}(s) \\ \hat{T}_{31}(a) \\ \hat{T}_{32}(a) \\ \hat{T}_{33}(a) \end{pmatrix} \quad [14a]$$

and

$$\frac{d}{dt}\begin{pmatrix} \hat{T}_{10} \\ \hat{T}_{11}(s) \\ \hat{T}_{21}(a) \\ \hat{T}_{22}(a) \\ \hat{T}_{30} \\ \hat{T}_{31}(s) \\ \hat{T}_{32}(s) \\ \hat{T}_{33}(s) \end{pmatrix} = -\begin{pmatrix} 0 & 0 & 0 & 0 & 0 & 0 & 0 & 0 \\ 0 & 3/5J_0 & 0 & 0 & 0 & \sqrt{6}/5J_0 & 0 & 0 \\ 0 & 0 & J_0 & 0 & 0 & 0 & 0 & 0 \\ 0 & 0 & 0 & J_0 & 0 & 0 & 0 & 0 \\ 0 & 0 & 0 & 0 & 0 & 0 & 0 & 0 \\ 0 & \sqrt{6}/5J_0 & 0 & 0 & 0 & 2/5J_0 & 0 & 0 \\ 0 & 0 & 0 & 0 & 0 & 0 & J_0 & 0 \\ 0 & 0 & 0 & 0 & 0 & 0 & 0 & 0 \end{pmatrix} \times \begin{pmatrix} \hat{T}_{10} \\ \hat{T}_{11}(s) \\ \hat{T}_{21}(a) \\ \hat{T}_{22}(a) \\ \hat{T}_{30} \\ \hat{T}_{31}(s) \\ \hat{T}_{32}(s) \\ \hat{T}_{33}(s) \end{pmatrix}. \quad [14b]$$

Therefore, the time dependence of the basis operators under the static Hamiltonian and considering the relaxation effects is given by the sum of Eqs. [10], [13], and [14]. The two sets of equations (the first set consisting on the sum of Eqs. [10a], [13a], and [14a] and the second set by the sum of Eqs. [10b], [13b], and [14b]) evolve independently, but are coupled at a change of RF phase by Eqs. [7a–7b]. Each set of differential equations is linear, and the matrices are symmetric. Once the eigenvalues and eigenvectors of these matrices are known, the time dependence of each of the basis vectors can be determined. Due to the large size of the matrices in these differential equations and to the fact that they are not very sparse, we have chosen to find numerical solutions to the master equation, as described under Methods.

### 2. Modeling of the Biological Sample

Biological systems are intrinsically complicated, with properties varying spatially and temporally. Following (*22*), we model the sample as composed of a multitude of domains; within each domain, the motion of the ions is rapid, contributing to the spectral densities $J_0$, $J_1$, and $J_2$ that determine the conventional transverse relaxation rates $T_{2f}$ and $T_{2s}$. The exchange between domains is considered negligible on a time scale exceeding the inverse line splittings and/or widths. All nuclei in the domain have the same relaxation times and, for simplicity, we will assume that all of the domains are characterized by the same relaxation times. In each domain, the 3/2-spin sodium nuclei experience a non-zero average EFG due to the anisotropic interaction of these ions with macromolecules, and to the nonrandom distribution of these macromolecules within each domain (the fluctuating part induces relaxation, see above). The residual EFGs are characterized by the principal value $\langle V_{zz}\rangle$ along the major axis (given by the domain orientation) and by the asymmetry parameter $\eta = (\langle V_{xx}\rangle - \langle V_{yy}\rangle)/\langle V_{zz}\rangle$. Therefore, each domain will be characterized by a static quadrupolar coupling $\omega_Q$ that depends on the orientation of the domain with respect to the main magnetic field $B_0$ (defined by the angles $\theta$ and $\phi$ below) (Eq. [15]) (*23*).

$$\omega_Q = \frac{eQ}{4\hbar}\langle V_{zz}\rangle(3\cos^2\theta - 1 + \eta\sin^2\theta\cos 2\phi) \quad [15]$$

In single crystals and macroscopically oriented liquid crystals, all of the domains have the same residual EFGs and are parallel (*24, 25*). If the ions/molecules are constrained within the domains and the domains are randomly oriented with respect to $B_0$ (but having the same residual EFGs and $\eta$), the NMR spectrum has the well-known "Pake powder" characteristics (*21, 26*). For poorly ordered samples, such as biological tissue, the domains are characterized by a wide distribution of $\langle V_{zz}\rangle$ and $\eta$ values. As can be shown by simulations, the resultant $\omega_Q$ distribution in such samples can be approximated as Gaussian (*22*). Consequently, we assumed that such a Gaussian distribution (Eq. [16]) is valid for our sample,

$$W(\omega_Q) = \frac{1}{\sqrt{2\pi}\,\sigma}\exp[-(\omega_Q - \bar{\omega}_Q)^2/2\sigma^2]. \quad [16]$$

Here, by $\bar{\omega}_Q$ we denote the average value of the static quadrupolar interaction parameter, while $\sigma$ denotes its second

moment, $\sigma^2 = \overline{(\omega_Q)^2}$. Generally, considering a distribution of static coupling constants $W(\omega_Q)$, the total NMR signal can be expressed as an integral over all the signals corresponding to different values of $\omega_Q$:

$$S_{\text{Total}} = \int W(\omega_Q) \cdot S(\omega_Q, \ldots) d\omega_Q. \quad [17]$$

## METHODS

As we have discussed above, the evolution of spin-3/2 nuclei under the influence of RF fields and static and fluctuating quadrupolar Hamiltonians is described by two sets of differential equations. The first set is given by the sum of Eqs. [10a], [13a], and [14a] and the second one by the sum of Eqs. [10b], [13b], and [14b]. These two sets evolve independently and are coupled at a change of RF phase by Eqs. [7a] and [7b].

The general matrix form of the two sets of equations is

$$\frac{dY}{dt} = MY. \quad [18]$$

Here $Y$ represents a complex vector of length 7 (first set) or 8 (second set), and $M$ a $7 \times 7$, $8 \times 8$, respectively, symmetric complex matrix. If we denote by $M_d$ the diagonal form of the matrix $M$ (obtained from the eigenvalues of $M$), and by $S$ the similarity transform (obtained from the eigenvectors of $M$), then $M_d = S^{-1} MS$, and the solution of Eq. [18] is

$$Y(t) = S \exp(M_d t) S^{-1} Y(0). \quad [19]$$

In this equation, $Y(0)$ represents the initial condition, and $\exp(M_d t)$ is the conventional notation for a $n$-dimensional square matrix ($n = 7$ or 8 in our case), with null nondiagonal elements and diagonal elements obtained from exponentiation of the eigenvalues of $M$ multiplied by time. For all of the experiments in this work, the initial density operator was proportional to the equilibrium state $\hat{T}_{10}$ (spins aligned along the main magnetic field). Mathematica (Wolfram Research, Champaign, IL) was used to obtain the numerical eigenvalues and eigenvectors of the evolution matrices, leading to the full time dependence of the basis elements. During the train of pulses, the RF strength was adjusted properly in time between 0 (RF off) and a value given by the ratio flip angle/pulse duration (RF on). The signal at the end of the train of RF pulses, assuming quadrature detection, is $I_x(t) + iI_y(t)$, being therefore proportional to the difference $\hat{T}_{11}(a) - \hat{T}_{11}(s)$. Consequently, the two sets of differential equations were solved for values of static quadrupolar interaction constants in the range $[\bar{\omega}_Q - 3\sigma, \bar{\omega}_Q + 3\sigma]$, and the corresponding signals were added together with the corresponding Gaussian weight function in order to obtain the total NMR signal.

## EXPERIMENTS

All of the experiments described below were performed on a commercial Bruker DMX-300 spectrometer (79.33-MHz sodium resonance frequency). A NMR instrument was used (instead of an imaging scanner) to overcome the software/hardware limitations that clinical systems impose on the shortest pulse widths that can be used for a hard 90° RF pulse (~400 $\mu$s). The extremely short RF pulses (12 $\mu$s) attainable with such a NMR spectrometer also allowed the unbiased determination of the relaxation rates. Since we do not expect the relaxation rates to vary significantly as the resonant frequency decreases from 79.33 to 33.78 MHz (the frequency of a 3-T imaging scanner), we benefited from performing our studies in a NMR spectrometer.

The sample was a small piece of bovine nasal cartilage, freshly received from the slaughterhouse (all of the experiments were conducted within 12 h of sacrificing the animal). To ensure a homogeneous radiofrequency field across the whole volume under study, the roughly cubic cartilage sample ($5 \times 5 \times 5$ mm) was placed in the center of a 10-mm NMR tube with the aid of small Teflon rods. The whole system (Teflon rods and sample) was immersed in $D_2O$, and the experiments were performed without spinning the sample.

Two sets of experiments were performed. The first one was used to characterize the sample and the second one to determine the triple-quantum signal loss as the RF pulse width was increased. The first set of experiments consisted of a TQ filter to determine the slow transverse relaxation time (equal to the relaxation time of the triple-quantum coherence (*27, 28*)) and of a double-quantum magic angle filter (DQ-MA) to determine $T_{2f}$ and the two parameters of the Gaussian distribution of quadrupolar coupling constants. We have assumed the sample to be homogeneously anisotropic, such that the pool of isotropic ions outside the extreme narrowing limit present in the sample was negligible. Therefore, the only ions contributing to both the TQ-filtered and the DQ-MA signal were the ions in anisotropic motion. Since in the presence of a non-zero average EFG the relations between transverse relaxation times and spectral density functions are (*20, 27, 29*)

$$\frac{1}{T_{2f}} = J_0(0) + J_1(\omega_0) + J_2(2\omega_0) \quad [20a]$$

and

$$\frac{1}{T_{2s}} = J_1(\omega_0) + J_2(2\omega_0), \quad [20b]$$

and assuming no high-frequency dispersion ($J_1 \approx J_2$), the two

relaxation times $T_{2s}$ and $T_{2f}$ completely determine the relevant spectral density functions.

### 1. Determination of Sample Characteristics

The triple-quantum relaxation rate was measured with the aid of a simple triple-quantum filtration experiment:

$$\left[\frac{\pi}{2}(\Phi) \xrightarrow{\tau/2} \pi(\Phi) \xrightarrow{\tau/2} \frac{\pi}{2}(\Phi + 90) \xrightarrow{\delta/2} \pi(\Phi + 90) \xrightarrow{\delta/2} \frac{\pi}{2}(0) - \text{acquire}\right]. \quad [2]$$

The second 180° pulse is not standard in a TQ-filtered sequence, but was needed in order to refocus the effects of the $B_0$ inhomogeneity as the evolution time was increased (*30*). The phase, $\Phi$, of the RF pulses was stepped through the values 30°, 90°, 150°, −150°, −90°, −30°, while the receiver's phase was toggled between the values 0° and 180° for consecutive scans. The preparation time, $\tau$, was kept constant ($\tau = 2.4$ ms), while the evolution time of the triple-quantum coherence, $\delta$, was varied stepwise (12 steps, with $\delta \in [0.4\text{ ms}, 12\text{ ms}]$), and the strength of the TQ-filtered signal was monitored. The pulse width of the 90° pulses was 12.4 $\mu$s, and the signals were placed on resonance. For each value of the evolution time, 360 signals were added together, with data points collected every 16 $\mu$s (4096 total number of data points), leading to a 43-s total experiment time. The TQ-filtered signals were integrated in time (the receiver was phased such that the entire signal was present only on one channel), and a monoexponential fit was consequently performed to the 12 data points to yield the triple-quantum coherence relaxation time.

A DQ-MA filter was used to determine the fast relaxation time of the sample, along with the two parameters of the Gaussian distribution, $\bar{\omega}_Q$ and $\sigma$. It consisted of the sequence of RF pulses:

$$\frac{\pi}{2}(\Phi) \xrightarrow{\tau/2} \pi(\Phi) \xrightarrow{\tau/2} 54.7°(\Phi) \xrightarrow{\delta} 54.7°(0) - (\text{acquire}). \quad [22]$$

The phase, $\Phi$, of the pulses was stepped through the values 0°, 90°, 180°, 270°, while the phase of the receiver was alternated between 0° and 180°. The evolution time, $\delta$, was kept very short (40 $\mu$s), and the preparation time, $\tau$, was varied in seven steps between 0.5 and 4 ms. The typical 90° pulse width was 12.4 $\mu$s. For each of the seven sets of data, 2400 scans were added (4.4-min total acquisition time), and each scan consisted of 1024 points (10-$\mu$s dwell time). Provided that the RF pulse widths are short compared to the transverse relaxation times, the signal at the end of the DQ-MA filter can be expressed as (*29*)

$$S(\omega_Q, \tau, t) \propto \sin(\omega_Q\tau)\sin(\omega_Q t)e^{-t/T_{2f}}e^{-\tau/T_{2f}}. \quad [23]$$

By integrating Eq. [23] over all of the possible $\omega_Q$ values, with the Gaussian weight function (Eq. [16]), Eq. [23] transforms to

$$S(\bar{\omega}_Q, \tau, t) \propto \{e^{-(t-\tau)^2\sigma^2/2}\cos[\bar{\omega}_Q(t-\tau)] - e^{-(t+\tau)^2\sigma^2/2}\cos[\bar{\omega}_Q(t+\tau)]\} \times e^{-t/T_{2f}}e^{-\tau/T_{2f}}. \quad [24]$$

A nonlinear fit of the DQ-MA data to Eq. [24], using the Levenberg–Marquardt algorithm, was used for every value of the preparation time to yield values for $\bar{\omega}_Q$, $\sigma$, and $T_{2f}$.

### 2. TQ-Filtered Signal Decay with the RF Pulse Widths

The TQ filter used for studying the effect RF pulse width on signal loss consisted of a series three RF pulses followed by data acquisition. This filter was chosen because it produced the best *overall* signal-to-noise in our clinical imaging experiments (*13*).

$$\frac{\pi}{2}(\Phi) \xrightarrow{\tau} \frac{\pi}{2}(\Phi + 90) \xrightarrow{\delta} \frac{\pi}{2}(0) - \text{acquire} \quad [25]$$

In order to obtain a triple-quantum signal, the phase $\Phi$ of the pulses was stepped through the values 30°, 90°, 150°, −150°, −90°, −30°, and consequent signals were added/subtracted together, corresponding to an alternation of the phase of the receiver between 0° and 180°. The preparation time $\tau$ was defined from the end of the first pulse up to the beginning of the second pulse and was kept at 2.4 ms for all of the experiments. The evolution time $\delta$ was defined from the end of the second pulse up to the beginning of the third pulse and had the value 0.02 ms throughout the experiments. The power levels for 90° flip angle were previously calibrated for each pulse width (nine values uniformly distributed in the range [0.1–0.9 ms]) by maximizing the single-quantum signal. The acquisition parameters for each pulse width experiment were: 600 fids added together, 4096 points/fid, 16-$\mu$s dwell time, 60-s total experiment time.

## RESULTS AND DISCUSSION

Figure 1 presents the time integrals of the 12 TQ-filtered signals (collected with different values of the evolution time)

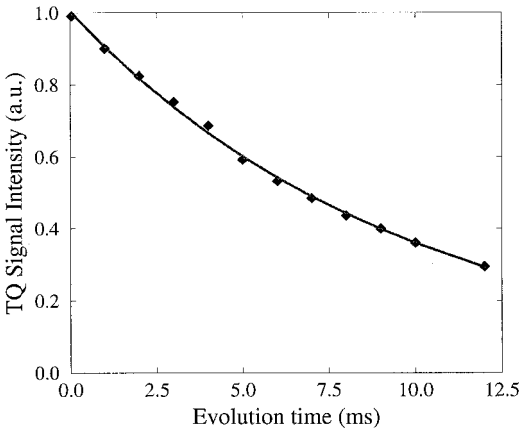


**FIG. 1.** Triple-quantum signal intensity as a function of evolution time. Diamonds represent experimental points (time integrals of the TQ signals) and the line represents the corresponding monoexponential fit. The result of the fit is the relaxation rate of the triple-quantum coherence, $T_{3Q} = 9.92$ ms.

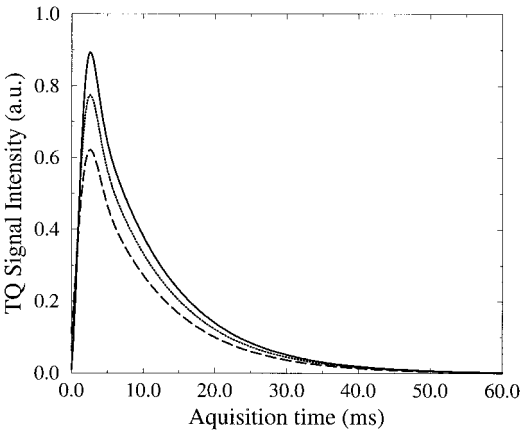


**FIG. 3.** Theoretical TQ signal intensity as a function of the acquisition time. The three curves correspond to RF pulse widths of 0.1 ms (solid), 0.5 ms (dotted), and 0.9 ms (dashed).

as a function of the evolution time. Because the RF pulses are extremely narrow, the TQ-filtered signal strength is monoexponentially decaying with the evolution time, and the decay time represents the relaxation time of the triple-quantum coherence. The diamonds represent the experimental data, while the line is the monoexponential fit. The relaxation time of the triple-quantum coherence obtained, equal to the slow transverse relaxation time, is $T_{3Q} = 9.92$ ms.

Figure 2 shows four of the seven experimental data sets collected with a double-quantum magic angle filter using preparation times of 0.5 ms (circles), 1.4 ms (up triangles), 3 ms (diamonds), and 4 ms (down triangles). Also presented in the same figure are the corresponding theoretical fits (Eq. [24])

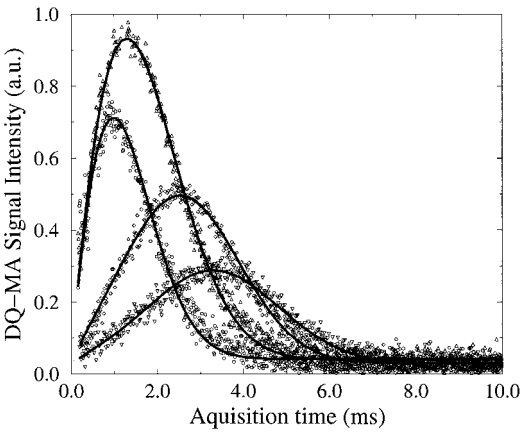


**FIG. 2.** DQ-MA signal intensity as a function of the acquisition time. The four sets of points shown correspond to four different values of the preparation time: $\tau = 0.5$ ms (circles), 1.4 ms (up triangles), 3 ms (diamonds), and 4 ms (down triangles). Along with the experimental data, the theoretical fits (Eq. [24]) are presented (smooth curves). The seven fits performed (of which only four are shown) yield the following sample characteristics: $T_{2f} = 3.5 \pm 0.93$ ms, $\bar{\omega}_Q = 0$ rad/s, $\sigma = 736.31 \pm 53.85$ rad/s.

(smooth lines). Using the DQ-MA data sets, the parameters characterizing the sample were found to be

$$\bar{\omega}_Q = 0 \text{ rad/s},$$

$$\sigma = 736.31 \pm 53.85 \text{ rad/s},$$

$$T_{2f} = 3.50 \pm 0.93 \text{ ms}. \qquad [26]$$

From the two transverse relaxation rates, $T_{2s}$ and $T_{2f}$, the two relevant density functions $J_0$ and $J_1$ can be determined, ($J_1 = 1/(2T_{2s})$ and $J_0 = 1/T_{2f} - 2J_1$), using Eqs. [20a] and [20b]. The two values obtained (considering the average value for $T_{2f}$) are, respectively, 0.0504 and 0.185 kHz for $J_1$ and $J_0$.

The analytic expressions used for the DQ-MA signal (Eqs. [23] and [24]) were deduced assuming a strong RF field ($\omega_1 \gg \omega_Q$) and slow exchange between different domains with respect to the inverse of the splitting. Since we have considered a static model (i.e., there is no exchange between the domains), the exchange rate is zero and satisfies the condition for observing the DQF-MA signal.

The values of $J_0$ and $J_1$ determined above allowed for the two sets of differential equations (Eq. [10] + Eq. [13] + Eq. [14]) to be solved numerically as described under Methods. Figure 3 presents three of these nine simulated TQ-filtered signals (Eq. [25]) for pulse widths of 0.1 ms (solid line), 0.5 ms (dotted line), and 0.9 ms (dashed line). For ensuing data sets, the strength of the RF pulses was decreased and the pulse widths increased, such that the product pulse width times pulse strength remained constant ($=\pi/2$). For each pulse width in the range [0.1–0.9 ms] (range relevant for clinical imaging applications) the static quadrupolar coupling parameter, $\omega_Q$, was varied between [−2200 rad/s, 2200 rad/s] in steps of 2 rad/s, and the resulting TQ-filtered signals were stored independently. Those signals were subsequently integrated with the

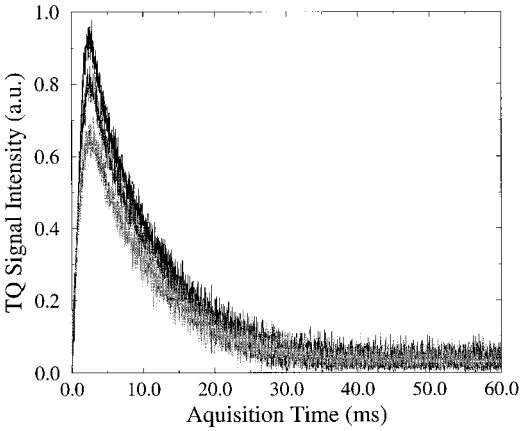


**FIG. 4.** Experimental TQ signal intensity as a function of acquisition time. The three curves shown correspond to RF pulse widths of 0.1 ms (top), 0.51 ms (middle), and 0.9 ms (bottom).

corresponding Gaussian weight function to yield a single, weighted TQ-filtered signal for each pulse width.

Figure 4 presents the magnitude for three of the nine experimental TQ-filtered signals collected with pulse widths of 0.1 ms (top), 0.51 ms (middle), and 0.9 ms (bottom) as described in the previous section. As can be noticed from Figs. 3 and 4, the simulated TQ-filtered signals and the TQ-filtered signals acquired experimentally are very similar. Most importantly, the theoretical simulations are not fits of the TQ-filtered experimental data, but were generated using the relaxation theory presented before by using only the sample characteristics ($J_0$, $J_1$, $\sigma$) as input. However, due to the fact that Fig. 4 displays the magnitude of the experimental TQ-filtered signals, there is a baseline which is not accounted for in the theoretical simulations (which are done in the high-temperature approximation, Fig. 3).

The accuracy of the model presented above to predict the TQ-filtered signal loss as the pulse width of the 90° RF pulses is increased can also be noticed when displaying the time integral of the TQ-filtered signals as a function of RF pulse width (Fig. 5). Here, the circles represent the time integrals of the experimental TQ-filtered signals, while the points generated by integrating the simulated signals were connected through a line. By repeating each experiment five times with the same acquisition parameters, the time integral of the signal varies on the order of 2%, so we estimate that the error in the experimental data presented in Fig. 5 is on the order of 2%. The set of data points and the theoretical curve are normalized such that they have equal value at the 0.5-ms data point. Our model indicates that a 15% increase in the sodium TQ-filtered signal strength is obtained as the pulse width of the hard 90° pulses are decreased from 500 to 100 $\mu$s. This prediction is in good agreement with the experimental results shown in Fig. 5.

The very simple domain model for the sodium ions in cartilage produces experimental results very close to the theoretical predictions. Since the triple-quantum signal is extremely weak, and because variations in the triple-quantum signal from human brain, cartilage, breast, etc., are suggested as being possibly connected to pathological conditions, an overall increase of 15% in the signal strength can be essential in perceiving important image details. However, this signal increase as the widths of the hard RF pulses are decreased is tightly connected to the properties of the tissue under study. It is known that the existence of the static quadrupolar interaction parameter influences the relaxation characteristics of the object under study. For example, it is customary to fit the TQ-filtered signal to a difference of two exponentials, with the results of the fits being $T_{2\text{rise}}$ and $T_{2\text{fall}}$. The relaxation time $T_{2\text{rise}}$ determines the signal behavior at small times, with $T_{2\text{fall}}$ governing the signal decay at long times. For narrow RF pulses, the exact TQ-filtered signal dependence on the conventional transverse relaxation rates, including the quadrupolar coupling constant $\omega_Q$, is (*22*)

$$TQ(t) \propto e^{-t/T_{2f}}\cos(\omega_Q t) - e^{-t/T_{2s}}. \qquad [27]$$

Therefore, the short-time signal behavior is modulated by $T_{2f}$ and the distribution of $\omega_Q$'s, and the long-time behavior is described by $T_{2s}$. As $T_{2\text{fall}}$ and $T_{2s}$ describe the same long-time signal behavior, we expect these two values not to be significantly different. However, since the $\omega_Q$ and $T_{2f}$ dependence are replaced by a single parameter ($T_{2\text{rise}}$) in the simpler biexponential fit, the $T_{2f}$ and $T_{2\text{rise}}$ values will most probably be different. For human cartilage $T_{2\text{rise}}$ values are measured to be in the submillisecond range (*31, 32*), while true values of $T_{2f}$ are shown to be consistently higher (*29*). The human brain

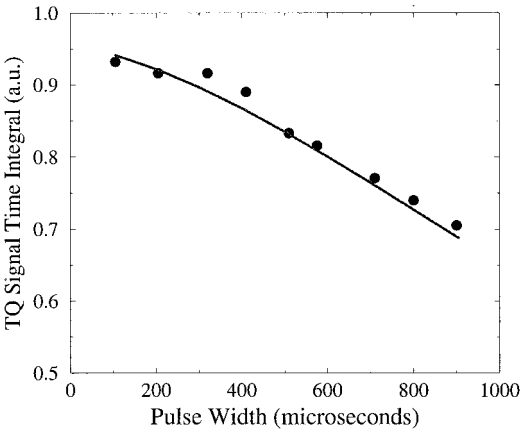


**FIG. 5.** TQ signal time integral as a function of RF pulse widths. Circles represent experimental data and the smooth curve the theoretical prediction. For nine RF pulse widths equally distributed in the interval [0.1–0.9 ms], TQ signals were obtained by numerically finding the solution of the sum Eqs. [10], [13], and [14] as described in the text. Each simulated TQ signal was consequently integrated in time, generating a single theoretical point. The nine theoretical points (joined by a line) and the experimental points are normalized such as they have equal value at the 0.5-ms time point.

yields values for $T_{2\text{rise}}$ in the range 2–4 ms. Since the brain is known for exhibiting quadrupolar splittings, too (*33*), we expect the true values of the fast relaxation times to be higher than the $T_{2\text{rise}}$ values, leading to smaller relaxation effects and smaller TQ-filtered signal increases with decreasing RF pulse widths. As a final conclusion, the TQ-filtered signal loss due to relaxation effects during the application of RF pulses can be predicted using the theory presented above. This signal loss is expected to be more significant for tissues characterized by faster relaxation rates (such as breast and cartilage) and less important for slower relaxing tissues (like brain). However, for the predictions of the theory to be accurate, the "true" relaxation times have to be previously measured, and also the distribution of static quadrupolar interaction constants has to be modeled and experimentally characterized for the tissue under study.

## CONCLUSIONS

We derived the equations describing the evolution of spins 3/2 in the presence of RF and both static and fluctuating quadrupolar interactions. A direct application of this theory was the study of signal loss in triple-quantum sodium MRI during RF excitation. The predictions from this theory were tested on a small piece of bovine nasal cartilage; this sample was modeled as composed of multiple domains, characterized by Gaussian-distributed static quadrupolar interaction constants. An increase of 15% in the TQ-filtered signal strength as the hard 90° RF pulse width was decreased from 500 to 100 $\mu$s was predicted and demonstrated experimentally.

## APPENDIX

The exact time dependence of the $\hat{T}_{20}$ evolution due to the presence of the static quadrupolar Hamiltonian $H_S^*$ can be deduced by diagonalizing the matrix in Eq. [10a]. The seven eigenvalues and eigenvectors are, respectively,

$$
\begin{aligned}
0 \quad A_1 &= \sqrt{\frac{5}{2}}\frac{\omega_1^2}{\omega_Q^2}\hat{T}_{11}(a) + \sqrt{\frac{3}{2}}\frac{\omega_1}{\omega_Q}\hat{T}_{22}(s) + \hat{T}_{33}(a)\\
0 \quad A_2 &= \left(\frac{5\omega_1^2}{\sqrt{6}\omega_Q^2} - \sqrt{\frac{2}{3}}\right)\hat{T}_{11}(a)\\
&\quad + \sqrt{\frac{5}{2}}\frac{\omega_1}{\omega_Q}\hat{T}_{22}(s)^{+} + \hat{T}_{31}(a)\\
0 \quad A_3 &= \sqrt{5}\frac{\omega_1}{\omega_Q}\hat{T}_{11}(a) + \hat{T}_{20}\\
\mp i\lambda_1 \quad A_{\mp 4} &= \sqrt{\frac{2}{5}}\frac{\omega_Q}{\omega_1}\hat{T}_{11}(a) - \sqrt{2}\,\hat{T}_{20} \mp \sqrt{\frac{2}{3}}\frac{\lambda_1}{\omega_1}\hat{T}_{21}(s)\\
&\quad - \sqrt{\frac{2}{3}}\left(1 + \frac{\omega_Q}{\omega_1}\right)\hat{T}_{22}(s)\\
&\quad + \frac{1}{\sqrt{15}}\left(5 + \frac{2\omega_Q}{\omega_1}\right)\hat{T}_{31}(a)\\
&\quad \pm \sqrt{\frac{2}{3}}\frac{\lambda_1}{\omega_1}\hat{T}_{32}(a) + \hat{T}_{33}(a)\\
\mp i\lambda_2 \quad A_{\mp 5} &= -\sqrt{\frac{2}{5}}\frac{\omega_Q}{\omega_1}\hat{T}_{11}(a) + \sqrt{2}\,\hat{T}_{20} \pm \sqrt{\frac{2}{3}}\frac{\lambda_2}{\omega_1}\hat{T}_{21}(s)\\
&\quad + \sqrt{\frac{2}{3}}\left(1 - \frac{\omega_Q}{\omega_1}\right)\hat{T}_{22}(s)\\
&\quad + \frac{1}{\sqrt{15}}\left(5 - \frac{2\omega_Q}{\omega_1}\right)\hat{T}_{31}(a)\\
&\quad \pm \sqrt{\frac{2}{3}}\frac{\lambda_2}{\omega_1}\hat{T}_{32}(a) + \hat{T}_{33}(a). \qquad \text{[A1]}
\end{aligned}
$$

The two symbols $\lambda_1$ and $\lambda_2$ are

$$
\begin{aligned}
\lambda_1 &= \sqrt{\omega_Q^2 + 2\omega_1\omega_Q + 4\omega_1^2}\\
\lambda_2 &= \sqrt{\omega_Q^2 - 2\omega_1\omega_Q + 4\omega_1^2}. \qquad \text{[A2]}
\end{aligned}
$$

With the eigenvalues and eigenvectors displayed before, the evolution of $\hat{T}_{20}$ under the static Hamiltonian is summarized as

**TABLE 1**

**Coefficients Giving the Exact Time Dependence of the Irreducible Operator $\hat{T}_{20}$ Due to the Presence of the Static Hamiltonian $H_S^*$ (Eq. [A3])**

$$
\begin{aligned}
a_{11}(t) \quad & -\frac{3\omega_1\omega_Q}{2\sqrt{5}}\left(\frac{\cos\lambda_1 t}{\lambda_1^2} + \frac{\cos\lambda_2 t}{\lambda_2^2} - \frac{\lambda_1^2+\lambda_2^2}{\lambda_1^2\lambda_2^2}\right)\\
a_{20}(t) \quad & \frac{\omega_Q^4 + \omega_1^2\omega_Q^2 + 4\omega_1^4}{\lambda_1^2\lambda_2^2} + \frac{3\omega_1^2}{2}\left(\frac{\cos\lambda_1 t}{\lambda_1^2} + \frac{\cos\lambda_2 t}{\lambda_2^2}\right)\\
a_{21}(t) \quad & -\frac{i\sqrt{3}\,\omega_1}{2}\left(\frac{\sin\lambda_1 t}{\lambda_1} + \frac{\sin\lambda_2 t}{\lambda_2}\right)\\
a_{22}(t) \quad & \frac{\sqrt{3}\,\omega_1}{2}\left[\omega_Q\left(\frac{\cos\lambda_1 t}{\lambda_1^2} - \frac{\cos\lambda_2 t}{\lambda_2^2}\right) + \omega_1\left(\frac{\cos\lambda_1 t}{\lambda_1^2} + \frac{\cos\lambda_2 t}{\lambda_2^2}\right)\right.\\
& \left. + \frac{2\omega_1}{\lambda_1^2\lambda_2^2}(\omega_Q^2 - 4\omega_1^2)\right]\\
a_{31}(t) \quad & -\frac{\sqrt{3}\,\omega_1}{2\sqrt{10}}\left[2\omega_Q\left(\frac{\cos\lambda_1 t}{\lambda_1^2} + \frac{\cos\lambda_2 t}{\lambda_2^2}\right) + 5\omega_1\left(\frac{\cos\lambda_1 t}{\lambda_1^2} - \frac{\cos\lambda_2 t}{\lambda_2^2}\right)\right.\\
& \left. - \frac{4\omega_Q}{\lambda_1^2\lambda_2^2}(\omega_Q^2 - \omega_1^2)\right]\\
a_{32}(t) \quad & \frac{i\sqrt{3}\,\omega_1}{2}\left(\frac{\sin\lambda_1 t}{\lambda_1} - \frac{\sin\lambda_2 t}{\lambda_2}\right)\\
a_{33}(t) \quad & -\frac{3\omega_1^2}{2\sqrt{2}}\left(\frac{\cos\lambda_1 t}{\lambda_1^2} - \frac{\cos\lambda_2 t}{\lambda_2^2} + \frac{\lambda_1^2-\lambda_2^2}{\lambda_1^2\lambda_2^2}\right)
\end{aligned}
$$

**TABLE 2**
**Coefficients Multiplying the Spin Operators in Eq. [A4a] in Terms of the $a_{ij}$ Coefficients Displayed in Table 1**

| $\sigma^*$ | $b_{11}$ | $b_{21}$ | $b_{22}$ | $b_{31}$ | $b_{32}$ |
|---|---|---|---|---|---|
| $\hat{T}_{11}(a)$ | $\frac{3}{5}a_{20}+\frac{\sqrt{3}}{5}a_{22}$ | $\frac{1}{\sqrt{5}}a_{32}$ | $\frac{1}{\sqrt{2}}a_{31}+\sqrt{\frac{3}{10}}a_{33}$ | $\frac{\sqrt{6}}{5}a_{20}+\frac{\sqrt{2}}{5}a_{22}$ | $\frac{1}{\sqrt{5}}a_{21}$ |
| $\hat{T}_{20}$ | $-\frac{3}{5}a_{11}-\frac{\sqrt{6}}{5}a_{31}$ | $-a_{21}$ | $-a_{22}$ | $-\frac{\sqrt{6}}{5}a_{11}-\frac{2}{5}a_{31}$ | $-a_{32}$ |
| $\hat{T}_{21}(s)$ | 0 | $a_{20}$ | 0 | 0 | $-\frac{1}{\sqrt{5}}a_{11}+\sqrt{\frac{3}{10}}a_{31}+\frac{1}{\sqrt{2}}a_{33}$ |
| $\hat{T}_{22}(s)$ | $-\frac{\sqrt{3}}{5}a_{11}+\frac{3}{5\sqrt{2}}a_{31}+\sqrt{\frac{3}{10}}a_{33}$ | 0 | $a_{20}$ | $-\frac{\sqrt{2}}{5}a_{11}+\frac{\sqrt{3}}{5}a_{31}+\frac{1}{\sqrt{5}}a_{33}$ | 0 |
| $\hat{T}_{31}(a)$ | $\frac{\sqrt{6}}{5}a_{20}-\frac{3}{5\sqrt{2}}a_{22}$ | $-\sqrt{\frac{3}{10}}a_{32}$ | $-\frac{1}{\sqrt{2}}a_{11}+\frac{1}{\sqrt{5}}a_{33}$ | $\frac{2}{5}a_{20}-\frac{\sqrt{3}}{5}a_{22}$ | $-\sqrt{\frac{3}{10}}a_{21}$ |
| $\hat{T}_{32}(a)$ | 0 | $-\frac{1}{\sqrt{5}}a_{11}+\sqrt{\frac{3}{10}}a_{31}+\frac{1}{\sqrt{2}}a_{33}$ | 0 | 0 | $a_{20}$ |
| $\hat{T}_{33}(a)$ | $-\sqrt{\frac{3}{10}}a_{22}$ | $-\frac{1}{\sqrt{2}}a_{32}$ | $-\sqrt{\frac{3}{10}}a_{11}-\frac{1}{\sqrt{5}}a_{31}$ | $-\frac{1}{\sqrt{5}}a_{22}$ | $-\frac{1}{\sqrt{2}}a_{21}$ |

$$e^{iH_S^*t}\hat{T}_{20}e^{-iH_S^*t} = a_{11}(t)\hat{T}_{11}(a) + a_{20}(t)\hat{T}_{20} + a_{21}(t)\hat{T}_{21}(s) + a_{22}(t)\hat{T}_{22}(s) + a_{31}(t)\hat{T}_{31}(a) + a_{32}(t)\hat{T}_{32}(a) + a_{33}(t)\hat{T}_{33}(a). \quad [A3]$$

The coefficients $a_{ij}$ are tabulated in Table 1. The spin operator double commutator for $m = 0$ can consequently be expressed as

$$[\hat{T}_{20}, [e^{-iH_S^*\tau}\hat{T}_{20}e^{iH_S^*\tau}, \sigma^*]] = b_{11}(\tau)\hat{T}_{11}(a)+b_{21}(\tau)\hat{T}_{21}(s) + b_{22}(\tau)\hat{T}_{22}(s) + b_{31}(\tau)\hat{T}_{31}(a) + b_{32}(\tau)\hat{T}_{32}(a) \quad [A4a]$$

for $\sigma^* = \{\hat{T}_{11}(a), \hat{T}_{20}, \hat{T}_{21}(s), \hat{T}_{22}(s), \hat{T}_{31}(a), \hat{T}_{32}(a), \hat{T}_{33}(a)\}$ and as

$$[\hat{T}_{20}, [e^{-iH_S^*\tau}\hat{T}_{20}e^{iH_S^*\tau}, \sigma^*]] = c_{11}(\tau)\hat{T}_{11}(s) + c_{21}(\tau)\hat{T}_{21}(a) + c_{22}(\tau)\hat{T}_{22}(a) + c_{31}(\tau)\hat{T}_{31}(s) + c_{32}(\tau)\hat{T}_{32}(s) \quad [A4b]$$

for $\sigma^* = \{\hat{T}_{10}, \hat{T}_{11}(s), \hat{T}_{21}(a), \hat{T}_{22}(a), \hat{T}_{30}, \hat{T}_{31}(s), \hat{T}_{32}(s), \hat{T}_{33}(s)\}$. The coefficients $b_{ij}$ and $c_{ij}$ are presented in Tables 2 and 3, respectively, in terms of the above tabulated $a_{ij}$'s. For calculating

**TABLE 3**
**Coefficients Multiplying the Spin Operators in Eq. [A4b] in Terms of the $a_{ij}$ Coefficients Displayed in Table 1**

| $\sigma^*$ | $c_{11}$ | $c_{21}$ | $c_{22}$ | $c_{31}$ | $c_{32}$ |
|---|---|---|---|---|---|
| $\hat{T}_{10}$ | $-\frac{\sqrt{3}}{5}a_{21}$ | $-\frac{\sqrt{3}}{5}a_{11}-\frac{\sqrt{2}}{5}a_{31}$ | $-\frac{2}{\sqrt{5}}a_{32}$ | $-\frac{\sqrt{2}}{5}a_{21}$ | $-\frac{2}{\sqrt{5}}a_{22}$ |
| $\hat{T}_{11}(s)$ | $\frac{3}{5}a_{20}-\frac{\sqrt{3}}{5}a_{22}$ | $-\frac{1}{\sqrt{5}}a_{32}$ | $\frac{1}{\sqrt{2}}a_{31}-\sqrt{\frac{3}{10}}a_{33}$ | $\frac{\sqrt{6}}{5}a_{20}-\frac{\sqrt{2}}{5}a_{22}$ | $\frac{1}{\sqrt{5}}a_{21}$ |
| $\hat{T}_{21}(a)$ | 0 | $a_{20}$ | 0 | 0 | 0 |
| $\hat{T}_{22}(a)$ | 0 | 0 | $a_{20}$ | 0 | 0 |
| $\hat{T}_{30}$ | $-\frac{2\sqrt{3}}{5}a_{21}$ | $-\frac{2\sqrt{3}}{5}a_{11}-\frac{2\sqrt{2}}{5}a_{31}$ | $\frac{1}{\sqrt{5}}a_{32}$ | $-\frac{2\sqrt{2}}{5}a_{21}$ | $\frac{1}{\sqrt{5}}a_{22}$ |
| $\hat{T}_{31}(s)$ | $\frac{\sqrt{6}}{5}a_{20}+\frac{3}{5\sqrt{2}}a_{22}$ | $\sqrt{\frac{3}{10}}a_{32}$ | $-\frac{1}{\sqrt{2}}a_{11}-\frac{1}{\sqrt{5}}a_{33}$ | $\frac{2}{5}a_{20}+\frac{\sqrt{3}}{5}a_{22}$ | $-\sqrt{\frac{3}{10}}a_{21}$ |
| $\hat{T}_{32}(s)$ | 0 | 0 | 0 | 0 | $a_{20}$ |
| $\hat{T}_{33}(s)$ | $-\sqrt{\frac{3}{10}}a_{22}$ | $-\frac{1}{\sqrt{2}}a_{32}$ | $-\sqrt{\frac{3}{10}}a_{11}-\frac{1}{\sqrt{5}}a_{31}$ | $-\frac{1}{\sqrt{5}}a_{22}$ | $-\frac{1}{\sqrt{2}}a_{21}$ |

the elements in these tables, the equality $\sqrt{3}\,a_{31} - \sqrt{2}\,a_{11} - \sqrt{5}\,a_{33} = 0$, easily deducible from Table 1, was also used.

With the aid of the tabulated $b_{ij}$ and $c_{ij}$ coefficients, the effect of the slowly fluctuating electric field gradients ($m = 0$ term) can be incorporated into the following set of differential equations:

The coefficients $A$ through $J$ are linear combinations of the spectral density functions $J_0(\lambda_1)$, $J_0(\lambda_2)$, and $J_0(0)$. The coefficients of these linear combinations are displayed in Table 4. Accordingly, the relaxation rates are sensitive to the spectral densities at low frequencies $\lambda_1$, $\lambda_2$, and 0. Two limiting situations are of special interest. In the absence of a low-frequency dispersion, i.e., when $J_0(0) \approx J_0(\lambda_1) \approx J_0(\lambda_2) = J_0$, the $\omega_Q$ and $\omega_1$ dependencies in the rates Eqs. [A5a] and [A5b] vanish and the relaxation matrices take the simple forms of Eqs. [14a] and [14b]. Furthermore, in the limit $\omega_1 = 0$, the time evolution can be solved in analytical form (*27*). In the limit $\omega_Q = 0$, but irrespective of a low-frequency dispersion, the rates agree with earlier results obtained in the doubly rotating tilted frame. In particular, it was shown that due to relaxation under (pulsed) RF triple-quantum coherences are excited, without a hard coherence transfer pulse (*34–36*).

$$\frac{d}{dt}\begin{pmatrix}\hat{T}_{11}(a)\\ \hat{T}_{20}\\ \hat{T}_{21}(s)\\ \hat{T}_{22}(s)\\ \hat{T}_{31}(a)\\ \hat{T}_{32}(a)\\ \hat{T}_{33}(a)\end{pmatrix} = -\begin{pmatrix} 3/10D & 0 & 0 & -\sqrt{15}/10E & \sqrt{6}/10D & 0 & 0\\ 3\sqrt{5}/10A & 0 & 0 & \sqrt{3}/2B & \sqrt{30}/10A & 0 & 0\\ 0 & 0 & 3/2G & 0 & 0 & 3/2F & 0\\ 3\sqrt{15}/10F & 0 & 0 & 3/2G & 3\sqrt{10}/10F & 0 & 0\\ 3\sqrt{6}/20I & 0 & 0 & 3\sqrt{10}/20J & 3/10I & 0 & 0\\ 0 & 0 & 3/2F & 0 & 0 & 3/2G & 0\\ 3\sqrt{10}/20B & 0 & 0 & \sqrt{6}/4A & \sqrt{15}/10B & 0 & 0\end{pmatrix}\begin{pmatrix}\hat{T}_{11}(a)\\ \hat{T}_{20}\\ \hat{T}_{21}(s)\\ \hat{T}_{22}(s)\\ \hat{T}_{31}(a)\\ \hat{T}_{32}(a)\\ \hat{T}_{33}(a)\end{pmatrix} \quad [A5a]$$

and

$$\frac{d}{dt}\begin{pmatrix}\hat{T}_{10}\\ \hat{T}_{11}(s)\\ \hat{T}_{21}(a)\\ \hat{T}_{22}(a)\\ \hat{T}_{30}\\ \hat{T}_{31}(s)\\ \hat{T}_{32}(s)\\ \hat{T}_{33}(s)\end{pmatrix} = -\begin{pmatrix} 0 & 0 & \sqrt{15}/10A & 0 & 0 & 0 & \sqrt{15}/5B & 0\\ 0 & 3/10C & 0 & -\sqrt{15}/10A & 0 & \sqrt{6}/10C & 0 & 0\\ 0 & 0 & 3/2G & 0 & 0 & 0 & 0 & 0\\ 0 & 0 & 0 & 3/2G & 0 & 0 & 0 & 0\\ 0 & 0 & \sqrt{15}/5A & 0 & 0 & 0 & -\sqrt{15}/10B & 0\\ 0 & 3\sqrt{6}/20H & 0 & 3\sqrt{10}/20A & 0 & 3/10H & 0 & 0\\ 0 & 0 & 0 & 0 & 0 & 0 & 3/2G & 0\\ 0 & 3\sqrt{10}/20B & 0 & \sqrt{6}/4A & 0 & \sqrt{15}/10B & 0 & 0\end{pmatrix}\begin{pmatrix}\hat{T}_{10}\\ \hat{T}_{11}(s)\\ \hat{T}_{21}(a)\\ \hat{T}_{22}(a)\\ \hat{T}_{30}\\ \hat{T}_{31}(s)\\ \hat{T}_{32}(s)\\ \hat{T}_{33}(s)\end{pmatrix}. \quad [A5b]$$

**TABLE 4**
**Coefficients Appearing in Eqs. [A5a] and [A5b] in Terms of the Spectral Density Functions $J_0(\lambda_1)$, $J_0(\lambda_2)$, and $J_0(0)$**

| | $J_0(\lambda_1)$ | $J_0(\lambda_2)$ | $J_0(0)$ |
|---|---|---|---|
| *A* | $\frac{\omega_1(\omega_Q+\omega_1)}{\lambda_1^2}$ | $\frac{\omega_1(\omega_Q-\omega_1)}{\lambda_2^2}$ | $-\frac{2\omega_1\omega_Q(\omega_Q^2+2\omega_1^2)}{\lambda_1^2\lambda_2^2}$ |
| *B* | $-\frac{\omega_1(\omega_Q+\omega_1)}{\lambda_1^2}$ | $\frac{\omega_1(\omega_Q-\omega_1)}{\lambda_2^2}$ | $-\frac{2\omega_1^2(\omega_Q^2-4\omega_1^2)}{\lambda_1^2\lambda_2^2}$ |
| *C* | $-\frac{\omega_1(\omega_Q-2\omega_1)}{\lambda_1^2}$ | $\frac{\omega_1(\omega_Q+2\omega_1)}{\lambda_2^2}$ | $\frac{2(\omega_Q^4+8\omega_1^4)}{\lambda_1^2\lambda_2^2}$ |
| *D* | $\frac{\omega_1(\omega_Q+4\omega_1)}{\lambda_1^2}$ | $-\frac{\omega_1(\omega_Q-4\omega_1)}{\lambda_2^2}$ | $\frac{2\omega_Q^2(\omega_Q^2+2\omega_1^2)}{\lambda_1^2\lambda_2^2}$ |
| *E* | $\frac{\omega_1(\omega_Q+4\omega_1)}{\lambda_1^2}$ | $\frac{\omega_1(\omega_Q-4\omega_1)}{\lambda_2^2}$ | $-\frac{2\omega_1\omega_Q(\omega_Q^2-4\omega_1^2)}{\lambda_1^2\lambda_2^2}$ |
| *F* | $-\frac{\omega_1^2}{\lambda_1^2}$ | $\frac{\omega_1^2}{\lambda_2^2}$ | $-\frac{4\omega_1^3\omega_Q}{\lambda_1^2\lambda_2^2}$ |
| *G* | $\frac{\omega_1^2}{\lambda_1^2}$ | $\frac{\omega_1^2}{\lambda_2^2}$ | $\frac{2}{3}\left[\frac{\omega_Q^4+\omega_Q^2\omega_1^2+4\omega_1^4}{\lambda_1^2\lambda_2^2}\right]$ |
| *H* | $\frac{\omega_1(\omega_Q+3\omega_1)}{\lambda_1^2}$ | $-\frac{\omega_1(\omega_Q-3\omega_1)}{\lambda_2^2}$ | $\frac{2}{3}\left[\frac{2\omega_Q^4+5\omega_Q^2\omega_1^2-4\omega_1^4}{\lambda_1^2\lambda_2^2}\right]$ |
| *I* | $-\frac{\omega_1(\omega_Q-\omega_1)}{\lambda_1^2}$ | $\frac{\omega_1(\omega_Q+\omega_1)}{\lambda_2^2}$ | $\frac{2}{3}\left[\frac{2\omega_Q^4-\omega_Q^2\omega_1^2+20\omega_1^4}{\lambda_1^2\lambda_2^2}\right]$ |
| *J* | $\frac{\omega_1(\omega_Q-\omega_1)}{\lambda_1^2}$ | $\frac{\omega_1(\omega_Q+\omega_1)}{\lambda_2^2}$ | $-\frac{2\omega_1\omega_Q(\omega_Q^2+6\omega_1^2)}{\lambda_1^2\lambda_2^2}$ |

## REFERENCES


1. S. Hilal, C. Oh, I. Mun, and A. Silver, Sodium imaging, *in* "Magnetic Resonance Imaging" (D. Stark and W. Bradley, Eds.), pp. 1091–1110, Mosby, St. Louis, 1992.
2. K. Thulborn, Quantitative multinuclear MR imaging and spectroscopy. *in* Abstracts of the Society of Magnetic Resonance in Medicine, New York p. 366 (1993).
3. J. W. C. van der Veen, P. van Gelderen, J. H. N. Creyghton, and W. M. M. J. Bovee, Diffusion in red blood cell suspensions: Sepa-

ration of the intracellular and extracellular NMR sodium signal, *Magn. Reson. Med.* **29,** 571–574 (1993).

4. J.-H. Lee, C. Labadie, and C. S. Springer, Relaxographic analysis of $^{23}$Na resonances, *in* Abstracts of the Society of Magnetic Resonance in Medicine, New York p. 2214 (1990).
5. R. K. Gupta and P. Gupta, Direct observation of resolved resonances from intra- and extra-cellular sodium-23 ions in NMR studies of intact cells and tissues using dysprosium (III) tripolyphosphate as paramagnetic shift reagent, *J. Magn. Reson.* **47,** 344–350 (1982).
6. N. Bansal, M. J. Germann, V. Seshan, G. T. Shires III, C. R. Malloy, and A. D. Sherry, Thulium 1,4,7,10-tetraazacyclododecane-1,4,7,10-tetrakis(methylene phosphate) as a $^{23}$Na shift reagent for the in vivo rat liver, *Biochemistry* **32**(21), 5638–5643 (1993).
7. V. Seshan, M. Germann, P. Preisig, C. Malloy, A. Sherry, and N. Bansal, TmDOTP5 as $^{23}$Na shift reagent for the in vivo rat kidney, *Magn. Reson. Med.* **34,** 25–31 (1995).
8. J. S. Tauskela, J. M. Dizon, J. Whang, and J. Katz, Evaluation of multiple-quantum-filtered $^{23}$Na NMR in monitoring intracellular Na content in the isolated perfused rat heart in the absence of a chemical shift reagent, *Magn. Reson. Med.* **127,** 115–127 (1997).
9. N. Bansal and V. Seshan, Three-dimensional triple quantum-filtered $^{23}$Na imaging of rabbit kidney with weighted signal averaging, *J. Magn. Reson. Imaging* **5,** 761–767 (1995).
10. R. Kalyanapuram, V. Sesham, and N. Bansal, Three-dimensional triple-quantum-filtered $^{23}$Na imaging of the dog head in vivo, *J. Magn. Reson. Imaging* **8,** 1182–1189 (1998).
11. V. Seshan, A. D. Sherry, and N. Bansal, Evaluation of triple quantum-filtered $^{23}$Na NMR spectroscopy in the in situ rat liver, *Magn. Reson. Med.* **38,** 821–827 (1997).
12. A. Borthakur, I. Hancu, F. Boada, G. Shen, E. Shapiro, and R. Reddy, In vivo triple quantum filtered twisted projection sodium MRI of human articular cartilage, *J. Magn. Reson.* **141,** 286–290 (1999).
13. I. Hancu, F. Boada, and G. Shen, Three-dimensional triple-quantum-filtered $^{23}$Na imaging of in vivo human brain, *Magn. Reson. Med.* **42**(6), 1146–1154 (1999).
14. F. Boada, J. Gillen, G. Shen, S. Chang, and K. Thulborn, Fast three dimensional sodium imaging, *Magn. Reson. Med.* **37,** 706–715 (1997).
15. G. Navon, Complete elimination of the extracellular $^{23}$Na NMR signal in triple quantum filtered spectra of rat hearts in the presence of shift reagents, *Magn. Reson. Med.* **30,** 503–506 (1993).
16. J. R. C. van der Maarel, The relaxation dynamics of spin $I = 1$ nuclei with a static quadrupolar coupling and a radio-frequency field, *J. Chem. Phys.* **99**(8), 5646–5653 (1993).
17. A. Abragam, "Principles of Nuclear Magnetism," Oxford Univ. Press, New York, 1978.
18. G. J. Bowden, W. D. Hutchinson, and J. Khachan, Tensor operator formalism for multiple-quantum NMR. Spins 3/2, 2 and 5/2 and general I, *J. Magn. Reson.* **67,** 415–437 (1986).
19. S. Chen and P. Rossky, Influence of solvent and counterion on $Na^{23+}$ spin relaxation in aqueous solution, *J. Phys. Chem.* **97**(41), 10803–10812 (1993).
20. L. Groot, J. R. C. van der Maarel, J. Leyte, $^{23}$Na relaxation in isotropic and anisotropic liquid-crystalline DNA solutions, *J. Phys. Chem.* **98,** 2699–2705 (1994).
21. W. D. Rooney and C. S. Springer Jr., A comprehensive approach to the analysis and interpretation of the resonances of spins 3/2 from living systems, *NMR Biomed.* **4,** 209–226 (1991).
22. D. Woessner and N. Bansal, Temporal characteristics of NMR signals from spin 3/2 nuclei of incompletely disordered systems, *J. Magn. Reson.* **133,** 21–35 (1998).
23. C. Slichter, "Principles of Magnetic Resonance," Springer-Verlag, New York, 1996.
24. A. Loewenstein and M. Brenman, Nuclear magnetic resonance of xenon-131 in a poly-$\gamma$-benzyl-L-glutamate liquid crystalline solution, *Chem. Phys. Lett.* **58,** 435–436 (1978).
25. W. Rooney, T. Barbara, and C. Springer, Two-dimensional double-quantum NMR spectroscopy of isolated spin 3/2 systems: $^{23}$Na examples, *J. Am. Chem. Soc.* **110,** 674–681 (1988).
26. H. J. Berendsen and H. T. Edzes, The observation and general interpretation of sodium magnetic resonance in biological material, *Ann. NY Acad. Sci.* **204,** 459–485 (1973).
27. J. R. C. van der Maarel, Relaxation of spin $S = 3/2$ in a nonzero average electric field gradient, *Chem. Phys. Let.* **155,** 288–296 (1989).
28. G. Jaccard, S. Wimperis, and G. Bodenhausen, Multiple-quantum NMR spectroscopy of $S = 3/2$ spins in isotropic phase: A new probe for multiexponential relaxation, *J. Chem. Phys.* **85,** 6282–6293 (1986).
29. U. Eliav and G. Navon, Analysis of double-quantum-filtered NMR spectra of $^{23}$Na in biological tissues, *J. Magn. Reson. B* **103,** 19–29 (1994).
30. R. Kemp-Harper, S. Brown, C. Hughes, P. Styles, and S. Wimperis, $^{23}$Na NMR methods for selective observation of sodium ions in ordered environments, *Prog. NMR Spectrosc.* **30,** 157–181 (1997).
31. A. Borthakur, I. Hancu, F. Boada, G. Shen, E. Shapiro, and R. Reddy, In vivo triple quantum filtered sodium MRI of human articular cartilage, *in* Abstracts of the Society of Magnetic Resonance in Medicine, p. 549 (1999).
32. U. Duvvuri, J. Leigh, and R. Reddy, Detection of residual quadrupolar interaction in the human breast in vivo using sodium-23 multiple quantum spectroscopy, *J. Magn. Reson. Imaging* **9,** 391–394 (1999).
33. R. Reddy, L. Bolinger, M. Shinnar, E. Noysewski, and J. Leigh, Detection of residual quadrupolar interaction in human skeletal muscle and brain in vivo via multiple quantum filtered sodium NMR spectra, *Magn. Reson. Med.* **33,** 134–139 (1995).
34. J. R. C. van der Maarel, Relaxation of spin $S = 3/2$ in the doubly rotating tilted frame, *J. Chem. Phys.* **91,** 1446–1450 (1989).
35. J. R. C. van der Maarel, R. Tromp, J. Leyte, J. Hollander, and C. Erkelens, Spin $S = 3/2$ $T1\rho$ relaxation, the excitation of triple-quantum coherences, *Chem. Phys. Let.* **169,** 585–590 (1990).
36. J. R. C. van der Maarel, Relaxation of spin quantum number $S = 3/2$ by multiple-pulse quadrupolar echoes, *J. Chem. Phys.* **94,** 4765–4775 (1991).